Applied Surface Science 627 (2023) 157256

Contents lists available at ScienceDirect

Applied Surface Science

journal homepage: www.elsevier.com/locate/apsusc

Full length article

Two-dimensional T′-phase MA_2N_4 (M=Mo/W, A=Si/Ge) nanosheets: First-principles insights into the structural stability, electronic property and catalytic performance for hydrogen evolution reaction

Yi Ding [a,*], Yanli Wang [b,*]

[a] School of Physics, Hangzhou Normal University, Hangzhou, Zhejiang 311121, People's Republic of China
[b] Department of Physics, Zhejiang Sci-Tech University, Hangzhou, Zhejiang 310018, People's Republic of China

ARTICLE INFO

Keywords:
MA_2N_4
Layered material
HER
First-principles calculations

ABSTRACT

For the emerging MA_2Z_4 materials, most researches focus on their perfect trigonal-prismatic (H-phase) and octahedral (T-phase) geometries, while the distorted octahedral (T′-phase) one is rarely studied. In this work, we perform a first-principles study on the T′-phase MA_2N_4 (M=Mo/W, A=Si/Ge) nanosheets to investigate their structural, mechanical, electronic and catalytic properties. As a metastable phase, the T′-MA_2N_4 nanosheets still possess sufficient stability from the energetic, dynamical, thermal and mechanical points of view. Unlike the semiconducting H-phase counterparts, the T′-MA_2N_4 nanosheets display a semimetallic or metallic behaviour depending on the lattice constants. Interestingly, these T′-MA_2N_4 nanosheets exhibit highly efficient catalytic performance for hydrogen evolution reaction (HER). The Gibbs free energy of hydrogen adsorption on the T′-$MoGe_2N_4$ nanosheet is close to zero, which is even superior to the well-known Pt catalyst. Furthermore, all the surface N atoms behave as active sites, giving rise to excellent basal HER activity. For these MA_2N_4 systems, the T′-phase will become more favourable than the H-phase via a combined effect of electron injection and tensile strain. Our study demonstrates that the T′-phase MA_2N_4 nanosheets possess peculiar electronic properties and promising HER activity, opening up potential applications in nano-devices and renewable energy.

1. Introduction

Since the discovery of $MoSi_2N_4$ nanosheets [1], layered MA_2Z_4 (M=transition-metal, A=Si/Ge, and Z=N/P/As) materials have attracted sufficient attention as a rising star in the field of physics, chemistry and material sciences [2–7]. Since there are no parent bulk structures for these MA_2Z_4 systems in nature, they are artificially fabricated by the chemical vapour deposition and reactive radio frequency magnetron sputtering methods in the experiments [1,8]. For the $MoSi_2N_4$ one, it is composed of septuple N-Si-N-Mo-N-Si-N atomic layers and can be regarded as a MoS_2-like MoN_2 nanosheet sandwiched between two buckled SiN surface layers [2,3]. The MoS_2-like semiconducting behaviour is also present in this $MoSi_2N_4$ system, which possesses a moderate gap size, high carrier mobilities and valley-dependent optical properties [9–11]. The band edges of $MoSi_2N_4$ nanosheet are originated from Mo *d* orbitals, which are localized in the central MoN_2 part [11,12]. Hence, these states will be protected by the SiN surface layers and become robust to external interference from foreign atoms and molecules [12,13]. Accompanied with the good air stability, the $MoSi_2N_4$ nanosheet is expected to be a promising channel material for sub-5-nm MOSFETs [14,15].

Besides the peculiar electronic properties, the $MoSi_2N_4$ nanosheet also exhibit the exciting application potential in clean and renewable energy industries. It is found that surface *N* vacancies can trigger the HER activity of $MoSi_2N_4$ nanosheet and the defective system exhibits a comparable HER performance to the Pt surface [16,17]. Non-precious transition metal atoms can be steadily anchored on the defect sites, forming efficient single-atom catalysts (SACs) not only for the HER [18,19], but also for the O_2 [20], NO [21,22], CO_2 [23] and N_2 [24] reduction reactions. It would be noted that the basal plane of $MoSi_2N_4$ nanosheet is inert to HER [16,17]. Thus, the number of activate sites is limited by the concentration of defects, which is normally small and hinders the practical catalytic applications. Utilizing the high-throughput calculations and symbolic transformer technology, it has been identified that pristine group-V_B MSi_2N_4 (M=V, Nb, Ta) systems possess basal catalytic activity for HER [25–27]. A detailed comparison between $MoSi_2N_4$ and $NbSi_2N_4$ nanosheets show that the metallic behaviour in the MA_2Z_4 system will improve the HER performance [27]. This strategy is validated in the strained $MoSi_2N_4$ system, where a large tensile strain can close its band gap and boost the HER activity [19].

* Corresponding authors.
E-mail addresses: dingyi2001@tsinghua.org.cn (Y. Ding), wangyanli-04@tsinghua.org.cn (Y. Wang).

https://doi.org/10.1016/j.apsusc.2023.157256
Received 2 March 2023; Received in revised form 7 April 2023; Accepted 10 April 2023
Available online 18 April 2023

It is worth mentioning that the investigated $MoSi_2N_4$ system is structurally analogous to the H-phase MoS_2 [6]. In addition to the H-phase, there also exists a metastable T′-phase in the MoS_2 system [28]. Such T′-MoS_2 nanosheet has a distorted octahedral coordination, which is formed by the dimerization of Mo atoms along the zigzag direction [29,30]. In the experiment, a large-scale preparation of T′-MoS_2 nanosheet has been reported [31]. Different from the H-phase, the T′-MoS_2 nanosheet exhibits an intriguing quantum spin Hall state [32]. Besides that, it also displays a good HER performance at the S atoms that connect the Mo dimers, where the hydrogen adsorption Gibbs free energy is less than 0.2 eV [33–36]. Such good HER activity of T′-MoS_2 nanosheet has been demonstrated in the experiments, endowing it promising catalytic applications [37,38]. Motivated by these progresses, we pay attention to the T′-phase geometry of $MoSi_2N_4$ and analogous systems. In this paper, we conduct a first-principles calculation to investigate the structural, mechanical, electronic, and catalytic properties of the T′-MA_2N_4 (M=Mo/W, A=Si/Ge) nanosheets. We find the T′-phase possesses sufficient stability and could exist in these MA_2N_4 systems. Unlike the H-phase counterparts, the T′-MA_2N_4 nanosheets are semimetallic/metallic and exhibit promising HER performance.

2. Computational details

The first-principles calculations are performed by the VASP code [39,40], which utilizes Perdew–Burke–Ernzerhof (PBE) projector-augmented wave pseudo-potentials and plane-wave basis sets with a cut-off energy of 500 eV. The Brillouin zone is sampled by a Wisesa–McGill–Mueller k-grid with minimum period distances of 35 and 50 Å in the relaxation and static calculations, respectively [41]. In order to simulate the isolated nanosheet, a vacuum layer of more than 15 Å is used. All the structural parameters are fully relaxed until the maximum residual force is less than 0.01 eV/Å. The post-processing of VASP data is done by the vaspkit code [42], and the bands of hybrid Heyd–Scuseria–Ernzerhof (HSE) calculations are obtained from the interpolation of Wannier functions [43]. The corresponding topological feature is further analysed by the Wanniertools code [44].

According to the computational hydrogen electrode model [45], the Gibbs free energy of hydrogen adsorption (ΔG_H^*) is evaluated as $\Delta G_H^* = E_H^* + \Delta E_{ZPE} - T\Delta S$. Here, E_H^* is the binding energy of H adatom, which is calculated as $E_H^* = E_H - E_P - \frac{1}{2}E_{H_2}$, where the E_H is the total energy of 2D system after the H adsorption, the E_P is the total energy of pristine system, and the E_{H_2} is the energy of an isolated H_2 molecule. The ΔE_{ZPE} and $T\Delta S$ terms are the differences of zero point energy and change of entropy for the H atom between the adsorbed state and gas phase, respectively. In order to precisely describe the bonding strength of H adatom, the D4 London dispersion correction is considered in the E_H^* and ΔE_{ZPE} calculations [46]. The entropy data of H_2 gas at the 298.15 K is obtained from the CRC handbook [47].

3. Results and discussion

Geometrical structure and energetic stability

First, the geometric characteristics of T′-phase MA_2N_4 nanosheets are investigated. The atomic structure of the T′-$MoSi_2N_4$ nanosheet is displayed in Fig. 1(a) as an example. Different from the H-phase, the T′-$MoSi_2N_4$ nanosheet has a rectangular lattice, which belongs to the $P2_1/m$ space group. The corresponding lattice constants are $a = 5.07$ and $b = 2.92$ Å, respectively, very close to the H-$MoSi_2N_4$ ones ($b = 2.91$ Å [11], and $a = \sqrt{3}b = 5.04$ Å for a hexagonal lattice). The central MoN_2 part of T′-$MoSi_2N_4$ nanosheet resembles the T′-MoS_2 one, where the Mo atoms are dimerized and form zigzag lines. Such metal dimerization can be observed in the scanning tunnelling microscope (STM) image as shown in Fig. 1(c). Under either negative or positive bias voltage, the bright points always appear on top of Mo atoms. There is a short Mo-Mo interatomic distance of d_1=2.68 Å within the same zigzag line, while the distance is enlarged to d_2=3.18 Å between different zigzag lines. The ratio d_1/d_2 can be used as an index of structural distortion in the T′-phase structures [48]. For the undistorted T-phase, the ratio d_1/d_2 is equal to 1, while it becomes less than 1 in the distorted T′-phase geometry. The smaller the ratio d_1/d_2, the more pronounced the structural distortion of system. Here, in the T′-$MoSi_2N_4$ nanosheet, the ratio d_1/d_2 is 0.85, which is bigger than the value (d_1/d_2=0.73) of T′-MoS_2. This indicates the structural distortion is weaker in the T′-$MoSi_2N_4$ nanosheet. It is consistent with the small buckling in the T′-$MoSi_2N_4$ nanosheet. For the inner N layers, i.e. the N atoms in the central MoN_2 part, the buckling height (Δh_i) is as small as 0.16 Å, which is much less than that of S atoms (0.40 Å) in the T′-MoS_2 system [29]. Such discrepancy between them is mainly attributed to the existence of outside SiN surface layers in the $MoSi_2N_4$ nanosheet, which will constrain the buckling of central MoN_2 part. In the surface SiN layers, the buckling height of outer N atoms (Δh_o) is further reduced to merely 0.05 Å for the T′-$MoSi_2N_4$ nanosheet. Such tiny value manifests that the outer N surfaces can be regarded as flat planes in the T′-$MoSi_2N_4$ one.

Table 1
The structural parameters of T′-MA_2N_4 nanosheets. For the comparison, the data of H-$MoSi_2N_4$, H-MoS_2 and T′-MoS_2 nanosheets are also listed.

	a (Å)	b (Å)	d_1 (Å)	d_2 (Å)	d_1/d_2	Δh_i (Å)	Δh_A (Å)	Δh_o (Å)
T′-$MoSi_2N_4$	5.07	2.92	2.68	3.18	0.84	0.16	0.14	0.05
T′-WSi_2N_4	5.09	2.92	2.67	3.20	0.83	0.19	0.15	0.05
T′-$MoGe_2N_4$	5.30	3.06	2.71	3.40	0.80	0.23	0.22	0.06
T′-WGe_2N_4	5.32	3.07	2.73	3.43	0.80	0.27	0.23	0.06
H-$MoSi_2N_4$	5.04	2.91	2.91	2.91	1	0	0	0
H-MoS_2	5.51	3.18	3.18	3.18	1	0	–	–
T′-MoS_2	5.72	3.18	2.77	3.80	0.73	0.40	–	–

The structural parameters of other T′-MA_2N_4 systems are listed in Table 1. It can be seen that the inorganic A element plays a more important role on the geometrical structures than the metal M one. For the same A component, the T′-WA_2N_4 nanosheets have analogous lattice constants, M-M distances and buckling heights to the T′-MoA_2N_4 ones. Whereas with the same M component, noticeable structural differences occur between T′-MSi_2N_4 and T′-MGe_2N_4 systems. Owing to the larger atomic radius of Ge atom than the Si one, the T′-MGe_2N_4 systems possess larger lattice constants and more pronounced structural distortions. The Δh_i rises to 0.23 and 0.27 Å in the T′-$MoGe_2N_4$ and T′-WGe_2N_4 nanosheets, respectively. Their Δh_o are still small to 0.06 Å as shown in Table 1, indicating the outer N surfaces of T′-MA_2N_4 systems are always flat regardless of the components.

To measure the energetic stability of T′-MA_2N_4 nanosheets, the cohesive energies (E_{coh}) are calculated as $E_{coh} = -(E_{MA_2N_4} - E_M - 2E_A - 4E_N)/7$. Here, $E_{MA_2N_4}$ is the total energy of MA_2N_4 nanosheet, and E_M, E_A, and E_N are the atomic energies of M, A, and N atoms at the spin-polarized state, respectively. Following this definition, the more positive the E_{coh} value, the more energetically favourable the structure. As shown in Fig. 1(d), among the four T′-phase systems, the T′-WSi_2N_4 one has the largest E_{coh} of 6.27 eV/atom, which is even bigger than that of H-$MoSi_2N_4$ system (6.12 eV/atom from the calculation with the same parameters). Although T′-$MoSi_2N_4$ and T′-WGe_2N_4 nanosheets have smaller E_{coh} values of 5.98 and 5.30 eV/atom, respectively, these data are still bigger than the H-MoS_2 one (5.11 eV/atom). The T′-$MoGe_2N_4$ system has the smallest E_{coh} of 5.01 eV/atom among the investigated systems, but it still exceeds the data of the T′-MoS_2 system (4.93 eV/atom). Since the H-$MoSi_2N_4$, H-MoS_2 and T′-MoS_2 nanosheets have already been fabricated in the experiments [1,31], the T′-MA_2N_4 nanosheets with comparable energetic stability are also experimentally accessible from the energetic point of view.

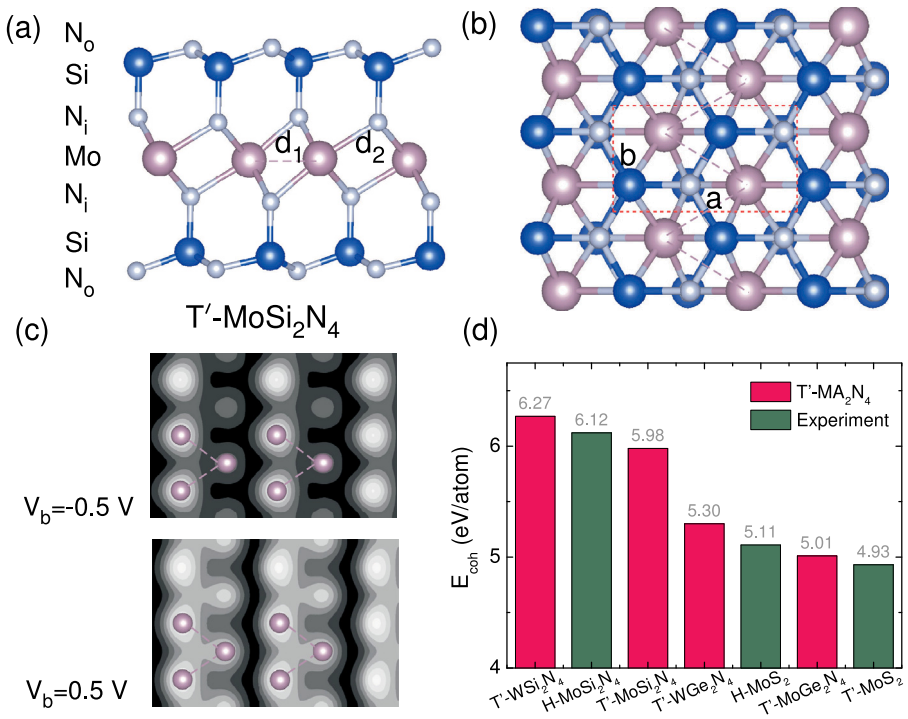

Fig. 1. [(a), (b)] The lateral and top views of T′-$MoSi_2N_4$ nanosheet. (c) The simulated STM images of T′-$MoSi_2N_4$ nanosheet under the negative/positive bias voltage of −0.5/0.5 V. The scanning distance is fixed to 2 Å above the surface. (d) The comparison of cohesive energies of T′-MA_2N_4 nanosheets and experimentally synthesized H-$MoSi_2N_4$, H- and T′-MoS_2 systems.

Dynamical and thermal stabilities

Now, we pay attention to the dynamical and thermal stabilities of T′-MA_2N_4 nanosheets. Phonon calculations are performed by the Phonopy code [49], which utilizes the force constants from the VASP calculations as the input. For the T′-$MoSi_2N_4$ nanosheet, both the finite displacement (FD) and density functional perturbation theory (DFPT) methods are used to obtain the force constants. The corresponding phonon dispersions based on the FD and DFPT results are displayed in Fig. 2(a). Two methods show the consistent phonon band structures with each other. Thus only the FD method is used for other T′-MA_2N_4 systems. It is worth mentioning that the smearing value (σ) in the FD/DFPT calculations will affect the lowest acoustic branch of the T′-$MoSi_2N_4$ nanosheet. When a small σ of 0.1 eV is adopted, small imaginary frequencies of about −30 and −60 cm^{-1} appear in the $S-\Gamma$ and $S-X$ lines. While as shown in Fig. 2(a) the imaginary frequencies are completely eliminated when σ is increased to 0.4 eV. In the literature, similar phenomenon has been reported in the 2D PbN nanosheet, where a large σ of 0.5 eV is required to obtain positive vibrational frequencies throughout the whole Brillouin zone [50]. Since the smearing value corresponds to an effective temperature for electrons [51], the imaginary frequencies in the small σ case implies that there will be a possible charge density wave (CDW) state at low temperature [50]. However, because the location of imaginary frequencies deviates from high symmetry points, a large supercell is needed to accommodate the CDW state, which will cost too many computational resources. On the other hand, all the vibrational frequencies become positive when a bigger σ value is used. This indicates a finite temperature will suppress the CDW state and enhance the stability of regular T′-phase geometry. Similarly, for other T′-MA_2N_4 systems, there are also no imaginary frequencies under the $\sigma = 0.4$ eV case. Therefore, it can be expected that the T′-phase geometrical structure will be present in the MA_2N_4 nanosheets at finite temperature.

To confirm the structural stability at finite temperatures, *ab initio* molecular dynamics (AIMD) simulation is further performed. It is carried out on a 2 × 3 supercell with a Nose thermostat at 500 K. The step time is set to 1 fs and the total simulation time is 10 ps, i.e. 10^4 steps. The variations of total energy and temperature during the AIMD simulations are displayed in Fig. 3 and the final configurations after the AIMD simulations are depicted in the insets. It can be seen that the energies are fluctuated around the equilibrium values without any sudden changes. Taking T′-$MoSi_2N_4$ as an example, the energy fluctuation during the last 5 ps is about 0.04 eV/atom, which is just comparable to the thermal fluctuation energy at 500 K ($k_BT \sim 0.043$ eV). The structural integrity is well kept in the final configuration without any broken bonds, and the mean squared displacements of Mo, Si and N atoms are only 0.08, 0.02 and 0.03 $Å^2$, respectively. Similar AIMD results are also obtained for other T′-MA_2N_4 systems as shown in Figs. 3(b)–(d), for which no structure destruction is observed. Thus, these T′-MA_2N_4 nanosheets can be inferred as stable 2D materials that maintain the free-standing state above room temperature.

Mechanical properties

Here, we investigate the mechanical properties of T′-MA_2N_4 nanosheets. The elastic moduli are calculated by the energy-vs.-strain method, where the elastic energy per unit of area (U) accumulated upon strain is expressed as $U = \frac{1}{2}C_{11}\varepsilon_{xx}^2 + \frac{1}{2}C_{22}\varepsilon_{yy}^2 + C_{12}\varepsilon_{xx}\varepsilon_{yy} + 2C_{44}\varepsilon_{xy}^2$ [52]. Through applying the uni-axial strain deformation along the armchair and zigzag directions (i.e. x and y directions), the U values can be simplified as $U = \frac{1}{2}C_{11}\varepsilon_{xx}^2$ and $U = \frac{1}{2}C_{22}\varepsilon_{yy}^2$, respectively. Thus, C_{11} and C_{22} of T′-$MoSi_2N_4$ nanosheet can be obtained from the $U-\varepsilon$ curves in Fig. 4(a), which are 491 and 449 N/m, respectively. These values are a little smaller than the H-$MoSi_2N_4$ one ($C_{11} = C_{22} = 533$ N/m [6]) but they are much larger than the T′-MoS_2 case (C_{11}=108, C_{22}=109 N/m [53]). When the biaxial strain deformation is applied to the T′-$MoSi_2N_4$ nanosheet, the U values can be expressed as $U = \frac{1}{2}(C_{11} + C_{22} + 2C_{12})\varepsilon_{xx}^2$ and the 2D stiffness ($C_{2D} = C_{11} + C_{22} + 2C_{12}$) is also obtained from the $U-\varepsilon$ curve, which is as large as 1180 N/m. This suggests the T′-$MoSi_2N_4$ nanosheet also possesses high stiffness akin to the H-phase counterpart. Based on

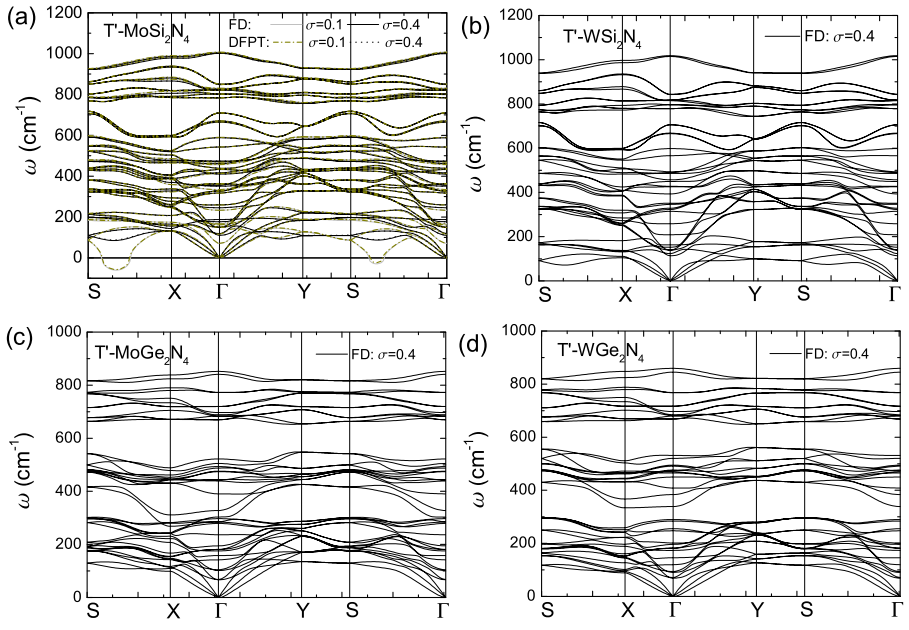

Fig. 2. The phonon dispersions of (a) T′-$MoSi_2N_4$, (b) T′-WSi_2N_4, (c) T′-$MoGe_2N_4$, and (d) T′-WGe_2N_4 nanosheets.

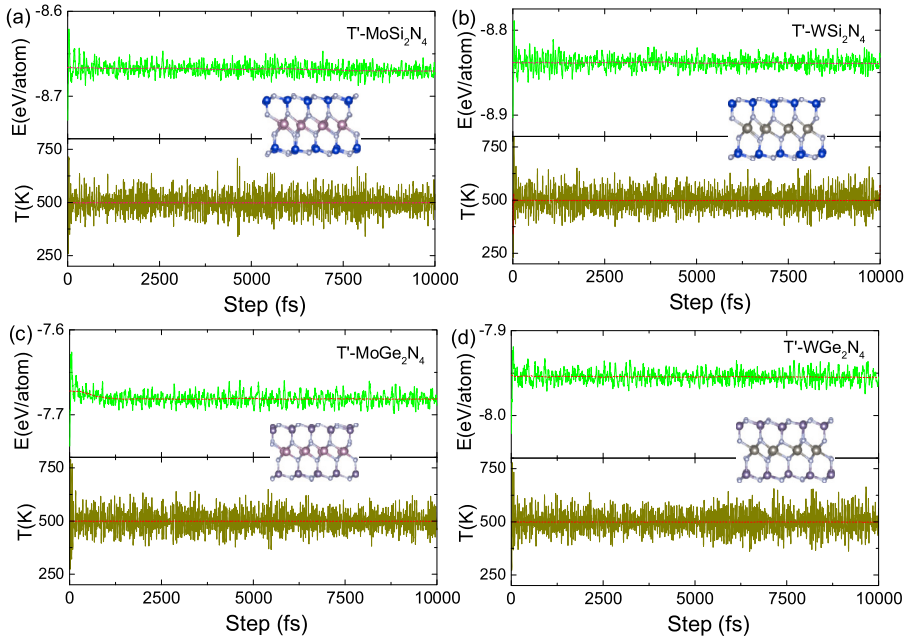

Fig. 3. The variations of total energies and temperatures versus the AIMD simulation steps for (a) T′-$MoSi_2N_4$, (b) T′-WSi_2N_4, (c) T′-$MoGe_2N_4$, and (d) T′-WGe_2N_4 nanosheets during the AIMD simulations. The final geometry after the AIMD simulation is also depicted in the insets.

the calculated C_{2D}, the C_{12} is obtained as 120 N/m and the gravity-induced out-of-plane deformation (h_d) can be further estimated as $h_d/L = \sqrt[3]{\rho g L/C_{2D}}$, where ρ is the density of 2D systems and L is the typical size of samples [54]. Following the convention of previous work [54,55], L is adopted as 100 μm and the h_d/L is estimated as 1.57×10^{-4} in the T′-$MoSi_2N_4$ nanosheet. This value is close to the H-$MoSi_2N_4$ one (1.50×10^{-4}) [6], indicating the T′-$MoSi_2N_4$ nanosheet would also withstand its own weight at the free-standing state. Finally, through applying shear deformation, the U values can be simplified as $U = 2C_{44}\varepsilon_{xy}^2$ and the C_{44} of T′-$MoSi_2N_4$ nanosheet is calculated to 170 N/m. For the T′-$MoSi_2N_4$ nanosheet, these obtained elastic moduli satisfy the Born–Huang criteria for an orthogonal lattice, i.e. C_{11}, C_{22}, C_{12}, $C_{44} > 0$ and $C_{11}C_{22} - C_{12}^2 > 0$ [56,57]. For other T′-MA_2N_4 nanosheets, their calculated elastic moduli are listed in Table 2, which also satisfy the Born–Huang criteria. Thus, it can be concluded that all the investigated T′-MA_2N_4 nanosheets are mechanically stable.

Utilizing the obtained elastic moduli, orientation dependent Young's modulus (Y) and Poisson's ratio (ν) of T′-MA_2N_4 nanosheets are evaluated as

$$Y(\theta) = \frac{\Delta}{C_{11}s^4 + C_{22}c^4 + (\Delta/C_{44} - 2C_{12})c^2s^2},$$

$$\nu(\theta) = -\frac{(C_{11} + C_{22} - \Delta/C_{44})c^2s^2 - C_{12}(c^4 + s^4)}{C_{11}s^4 + C_{22}c^4 + (\Delta/C_{44} - 2C_{12})c^2s^2},$$

where $\Delta = C_{11}C_{22} - C_{12}^2$, $c = cos\theta$ and $s = sin\theta$ (θ is the angle relative to the x axis, i.e. the armchair direction) [52]. The calculated Y and ν data are illustrated in Figs. 4(b) and (c). For the T′-$MoSi_2N_4$ nanosheet, Y is varied in the range of [420, 459] N/m with the minimum and

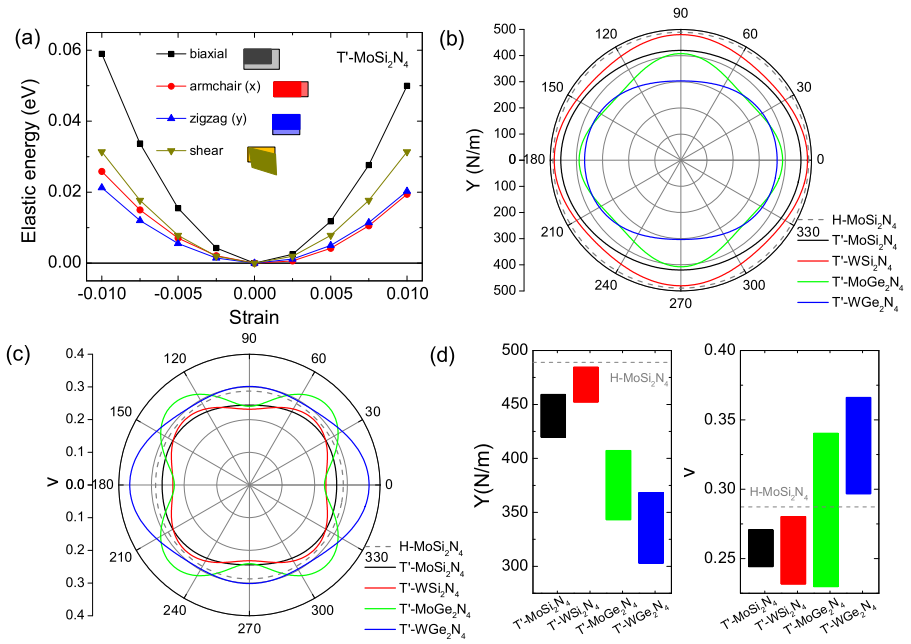

Fig. 4. (a) The variation of elastic energies with respect to the different types of strain deformations on the T′-$MoSi_2N_4$ nanosheet. (b) The orientation dependent Young's modulus (Y) and (c) Poisson's ratio (ν) of T′-MA_2N_4 nanosheets. (d) A comparison of the mechanical properties between the T′-MA_2N_4 and H-$MoSi_2N_4$ nanosheets.

Table 2
Mechanical properties of T′-MA_2N_4 nanosheets.

	C_{11} (N/m)	C_{22} (N/m)	C_{12} (N/m)	C_{44} (N/m)	C_{2D} (N/m)	h_d/L 10^{-4}	Y_{min} (N/m)	Y_{max} (N/m)	ν_{min}	ν_{max}
T′-$MoSi_2N_4$	491	449	120	170	1180	1.57	420	459	0.24	0.27
T′-WSi_2N_4	512	508	119	177	1250	1.73	452	485	0.23	0.28
T′-$MoGe_2N_4$	411	431	99	128	1040	1.80	343	407	0.23	0.34
T′-WGe_2N_4	414	340	125	132	1004	1.98	303	368	0.30	0.37

maximum values appearing in the $\theta = 90°$ and 0°, respectively. Due to the smaller elastic moduli, the T′-phase structure has a smaller Young's modulus than the H-phase $MoSi_2N_4$ (Y=490 N/m) [6]. In comparison to the Mo-based system, the T′-WSi_2N_4 nanosheet has a larger Y with the maximum (minimum) value of 484 (452) N/m in the $\theta = 0°$ ($\theta = 45°$) direction. For the T′-MGe_2N_4 nanosheets, the elastic moduli are smaller than the Si-based ones. As a result, the T′-$MoGe_2N_4$ and T′-WGe_2N_4 nanosheets have smaller Y values of [343, 407] and [303, 368] N/m, respectively. Note that the variations of Y in the T′-MGe_2N_4 nanosheets are much prominent than the T′-MSi_2N_4 ones, indicating the anisotropy is more pronounced in these Ge-based systems. Similar results hold true for ν, which varies more evidently in the T′-MGe_2N_4 nanosheets than the T′-MSi_2N_4 ones as shown in Fig. 4(d).

Electronic properties

Now, we focus on the electronic properties of T′-MA_2N_4 nanosheets, for which both the PBE and HSE band structures are depicted in Fig. 5. Different from the semiconducting H-phase ones [58], the T′-MSi_2N_4 nanosheets exhibit a semimetallic feature in their PBE bands. The valence band maximum is slightly higher (lower) than the conduction band minimum in the M=Mo (W) case. Analogous band dispersions are present in the HSE bands as shown in Figs. 5(a) and (b), where only a tiny band gap of 0.06 and 0.13 eV is present in the T′-$MoSi_2N_4$ and T′-WSi_2N_4 systems, respectively. Such gap sizes are much narrower than the H-phase counterparts (H-$MoSi_2N_4$: 2.29 eV, H-WSi_2N_4: 2.66 eV) [6], which makes these T′-MSi_2N_4 nanosheets can be viewed as semimetals. Moreover, the band gaps of T′-$MoGe_2N_4$ and -WGe_2N_4 nanosheets are completely closed in both PBE and HSE bands. As shown in Figs. 5(c) and (d), their bottom conduction and top valence bands are overlapped and become partially occupied, which gives rise to a typical metallic behaviour in these T′-MGe_2N_4 systems.

To shed light on the semimetallic/metallic behaviours of T′-MA_2N_4 systems, the partial density of states (PDOSs) and orbital-projected fat-band analysis are performed on the T′-WSi_2N_4 nanosheet. As shown in Figs. 6(a) and (b), the states around the Fermi level are primarily from the W and N atoms, while the contribution of Si atoms is marginal. The W d_{xz} and d_{z2} orbitals dominate the top valence and bottom conduction bands around the Γ point, respectively. It is found that the band gap of T′-WSi_2N_4 nanosheet depends strongly on the lattice constants. As displayed in Fig. 6(c), the compressive strain, which shortens the lattice constants, can enlarge the gap size, while the tensile strain will reduce it. For the T′-WSi_2N_4 nanosheet, when the lattice constants are enlarged under a tensile strain of 0.04, the top valence and bottom conduction bands are overlapped, which leads to a metallic band feature analogous to the T′-WGe_2N_4 one. The band structures of other T′-MA_2N_4 systems are displayed in Fig. S2 of supplementary material. It can be seen that the metallic behaviours become more pronounced when tensile strains are applied. Contrarily, under the compressive strain, small band gaps of about 0.01~0.03 eV are opened in the T′-$MoSi_2N_4$, T′-$MoGe_2N_4$ and T′-WGe_2N_4 nanosheets under strains of −0.02, −0.06 and −0.05, respectively. Thus, akin to the H-phase $MoSi_2N_4$ and analogous systems [59], the relative energies of different d orbitals can be modulated by changing the lattice constants of T′-MA_2N_4 nanosheets. With smaller lattice constants, the T′-MSi_2N_4 systems exhibit a semimetallic feature, and the T′-MGe_2N_4 ones with bigger lattice constants will present a metallic behaviour.

It has been reported that the T′-MoS_2 nanosheet is a topological insulator with a non-trivial band gap near the Γ point when the spin-orbital coupling (soc) effect is considered [32]. To examine whether such non-trivial topological feature exists in the semimetallic T′-MSi_2N_4

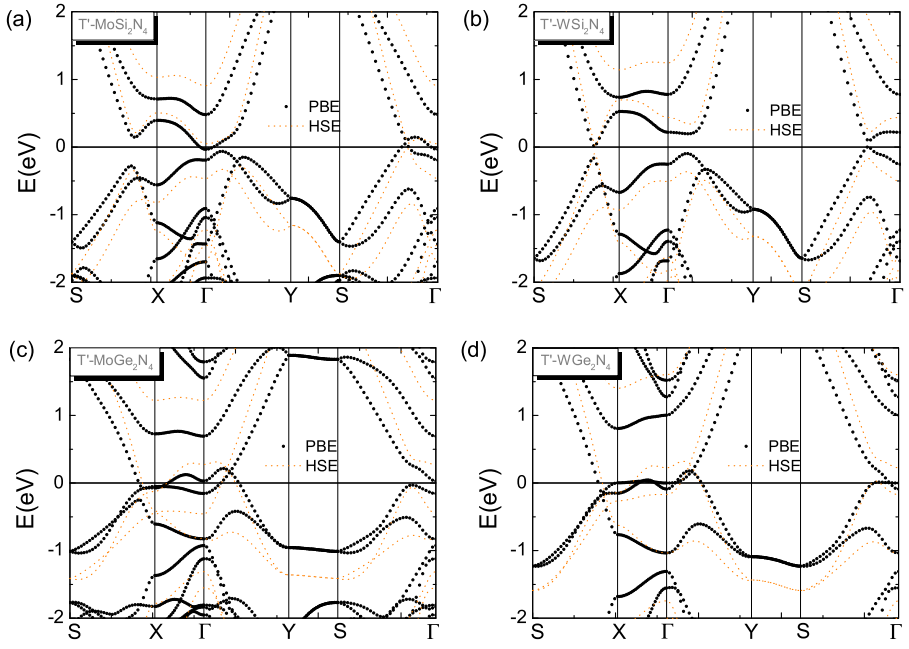

Fig. 5. The PBE and HSE band structures of (a) T′-$MoSi_2N_4$, (b) T′-WSi_2N_4, (c) T′-$MoGe_2N_4$, (d) T′-WGe_2N_4 nanosheets.

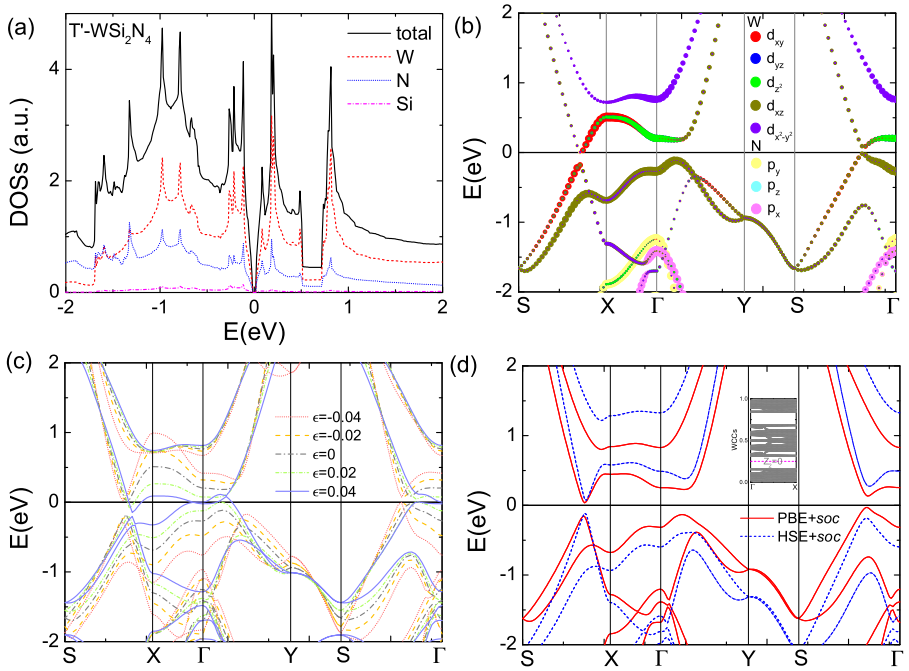

Fig. 6. (a) The partial densities of states and (b) orbital-projected fat bands of T′-WSi_2N_4 nanosheet. (c) The band structures of strained T′-WSi_2N_4 nanosheet by the PBE calculation. (d) Both the PBE+*soc* and HSE+*soc* band structures of strain-free T′-WSi_2N_4 nanosheet. The corresponding evolution of Wannier charge centres based on the HSE+*soc* result is depicted in the inset.

nanosheets, the PBE+*soc* and HSE+*soc* calculations are carried out. As displayed in Fig. 6(d), the PBE+*soc* and HSE+*soc* bands resemble the ones without *soc*. Based on the HSE+*soc* result, the Wannier charge centres (WCCs) calculation is further performed as shown in the inset of Fig. 6(d). The evolution of WCCs shows that an arbitrary horizontal reference line crosses the WCCs zero or even times, which indicates the Z_2 invariant is 0 for the T′-WSi_2N_4 nanosheet. The same result has also been obtained for the T′-$MoSi_2N_4$ nanosheet. Thus, the T′-WSi_2N_4 and T′-$MoSi_2N_4$ systems only have a trivial topological feature, which is different from the T′-MoS_2, T′-WS_2, T′-WSi_2P_2 and T′-WSi_2As_2 ones [32,60]. However, similar trivial feature has also been reported in the free-standing T′-MoN_2 and T′-WN_2 nanosheets [61]. This is mainly attributed to the greater electronegativity of *N* element than the S and P ones and the *N p* states locate in the deep valence bands of the N-based systems. As a result, the *d* – *p* band inversion is absent around the Fermi level and the T′-MA_2N_4 nanosheets are ordinary semimetals or metals.

Catalytic properties

For the T′-MA_2N_4 nanosheets, the absolute energies of band edges, which adopt the vacuum level as the zero point, are calculated as

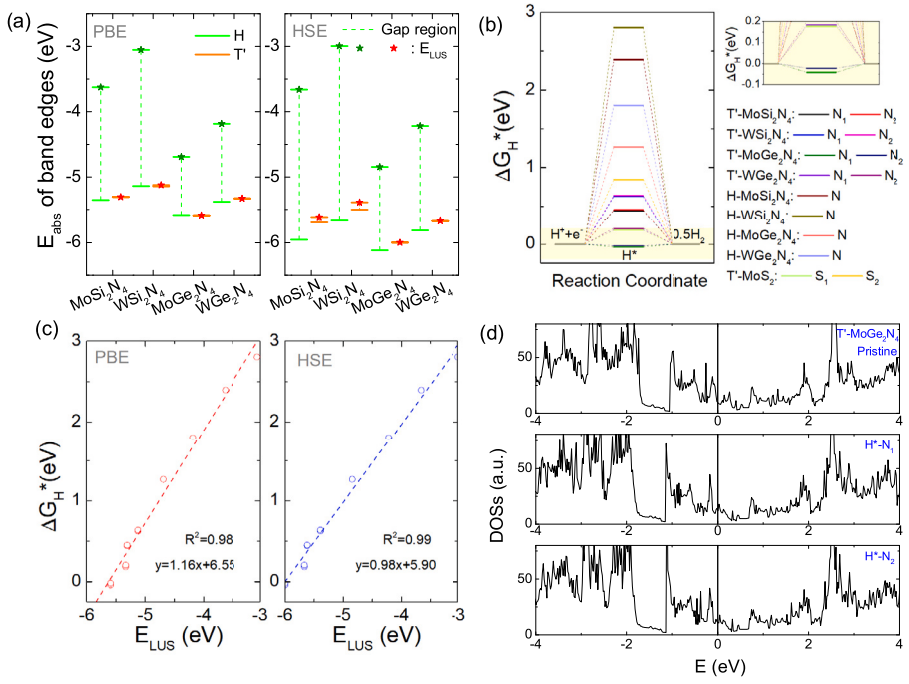

Fig. 7. (a) The absolute energies of band edges in the T′- and H-MA_2N_4 (M=Mo/W, A=Si/Ge) nanosheets. The gap region and the energies of lowest unoccupied state (E_{LUS}) are also marked. (b) The Gibbs free energy diagram of HER processing on the T′- and H-MA_2N_4 nanosheets as well as the T′-MoS_2 one. (c) The relation between the ΔG_H^* and E_{LUS}. (d) The densities of states of T′-WGe_2N_4 nanosheet before and after the H adsorption.

shown in Fig. 7(a). It can be seen that in comparison to the H-phase ones, the absolute energies of the lowest unoccupied state (E_{LUS}), i.e. the conduction band minimum of semiconductors or the Fermi level of metals, are much lower in the T′-MA_2N_4 systems. The PBE/HSE calculations indicate the E_{LUS} of T′-MA_2N_4 ones are in the range of [−5.6, −5.3]/[−6, −5.3] eV, which are very close to the valence band maximum of H-phase counterparts. Moreover, these E_{LUS} values are below the redox potential of H^+/H_2 (−4.44 eV), which is a good signal for the high HER activity [27]. Hence, we further investigate the HER catalytic behaviour of T′-MA_2N_4 nanosheets.

For sake of comparison, the Gibbs free energies of hydrogen adsorption (ΔG_H^*) are firstly calculated for the H-phase MA_2N_4 systems. The obtained ΔG_H^* values are 2.39 and 2.80 eV on the H-$MoSi_2N_4$ and H-WSi_2N_4 nanosheets, respectively, which agree well with previous studies (H-$MoSi_2N_4$: 2.27–2.51 eV [16–19] and H-WSi_2N_4: 2.79 eV [16]). Smaller ΔG_H^* data of 1.27 and 1.80 eV are obtained for the H-$MoGe_2N_4$ and H-WGe_2N_4 nanosheets, respectively, but they are still too big for an effective HER catalyst that should satisfy the condition of $|\Delta G_H^*| < 0.2$ eV [26,27]. This means the H atoms are weakly bound on the H-phase MA_2N_4 systems, which only exhibit an inertial HER activity. For the T′-MA_2N_4 nanosheets, it is found that the H atoms prefer to bind with the surface N atoms akin to the H-phase systems [16]. Fig. 7(b) further displays ΔG_H^* of T′-MA_2N_4 systems, which are much smaller than the H-phase ones. Owing to the low symmetry of T′-phase structure, there will be two inequivalent surface *N* sites for the H adatoms, i.e. N_1 and N_2 ones as illustrated in Fig. 8(a). For the T′-$MoSi_2N_4$ and T′-WSi_2N_4 nanosheets, their ΔG_H^* data are 0.44/0.45 and 0.63/0.64 eV at the N_1/N_2 site, respectively, and the values drop to −0.04/−0.02 and 0.18/0.20 eV in the T′-$MoGe_2N_4$ and T′-WGe_2N_4 systems. It demonstrates that the T′-MGe_2N_4 systems satisfy the criterion of $|\Delta G_H^*| < 0.2$ and will exhibit good HER performance. In particular, the ΔG_H^* of T′-$MoGe_2N_4$ nanosheet is close to the ideal zero point, which is even superior to the well-known Pt catalyst ($\Delta G_H^* = -0.09$ eV). Therefore, the T′-$MoGe_2N_4$ nanosheet will be a promising candidate for the highly efficient HER catalyst.

In order to understand the physical origin for the excellent HER performance, the density of states (DOSs) of T′-$MoGe_2N_4$ systems before and after the H adsorption are displayed in Fig. 7(d). It can be seen that the DOSs of T′-$MoGe_2N_4$ nanosheet are not disrupted by the H adatoms, which just upshift the Fermi level slightly. By the Bader charge analysis [62], it is found that the H adatom transfers about 0.3 *e* to the T′-$MoGe_2N_4$ nanosheet, which will fill the lowest unoccupied states. Hence, the E_{LUS} data of pristine system will be a key factor for the binding strength of H adatom [27]. To confirm this speculation, the functions of ΔG_H^* versus E_{LUS} are depicted in Fig. 7(c). There is a linear relationship between them, which can be fitted as $\Delta G_H^* = 1.16 \times E_{LUS} + 6.55$ ($\Delta G_H^* = 0.98 \times E_{LUS} + 5.90$) for the PBE (HSE) result. According to this equation, when the PBE (HSE) E_{LUS} value is around −5.7 (−6.0) eV, the corresponding ΔG_H^* data will touch the ideal zero point. Here, among the investigated T′-MA_2N_4 systems, the T′-$MoGe_2N_4$ nanosheet possesses the optimal E_{LUS} value, which is responsible for its excellent HER performance.

For the T′-$MoGe_2N_4$ nanosheet, the influence of H concentration on ΔG_H^* is further examined by changing the size of supercell. As shown in Fig. 8(b), the ΔG_H^* values are slowly raised with the increase of H concentration. When the H concentration reaches up to 25%, the ΔG_H^* of T′-$MoGe_2N_4$ nanosheet still satisfies the condition of $|\Delta G_H^*| < 0.2$ eV. Comparing to the data of defective H-$MoSi_2N_4$ system [17], the valid H concentration for the HER activity is much wider in the T′-$MoGe_2N_4$ nanosheet as shown in Fig. 8(b), indicating it will be more suitable for real applications. Besides that, the ΔG_H^* difference between the N_1 and N_2 sites is always less than 0.01 eV regardless of the H concentration. It means all the surface *N* atoms of T′-$MoGe_2N_4$ nanosheet will behave as active sites for the HER. This is superior to the T′-MoS_2 system, where only half of the surface S atoms are active to the HER [36]. Consistent with previous study [36], our calculation shows that the S atoms that connect the Mo dimers (S_1 site) has a moderate ΔG_H^* of 0.18 eV, while ΔG_H^* is raised to 0.85 eV at the S atoms that link adjacent Mo zigzag lines (S_2 site). The big difference between S_1 and S_2 sites is attributed to the remarkable buckling in the surface S layers (0.40 Å). Whereas in the T′-$MoGe_2N_4$ nanosheet, the buckling of outer N layers is negligible and both N_1 and N_2 atoms possess similar HER performance. Thus, the T′-$MoGe_2N_4$ nanosheet possess a promising basal catalytic activity for HER.

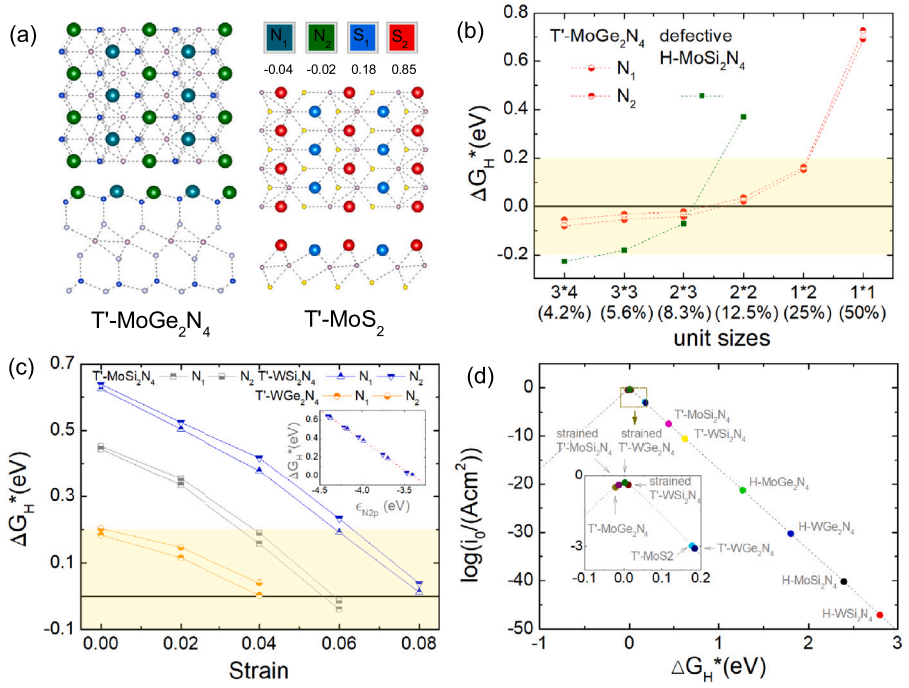

Fig. 8. (a) The distribution of the ΔG_H^* on the different surface sites of T′-$MoGe_2N_4$ and T′-MoS_2 nanosheets. (b) The variations of ΔG_H^* versus the used supercell sizes of T′-$MoGe_2N_4$ and defective H-$MoSi_2N_4$ nanosheets. (c) The variations of ΔG_H^* of T′-WGe_2N_4 T′-$MoSi_2N_4$ and T′-WSi_2N_4 systems under the homogeneous tensile strains. The inset depicts the variations of ΔG_H^* versus the p-band centre of N atoms (ϵ_{N-2p}). (d) The volcano curve of $log(i_0)$ versus ΔG_H^* for the investigated T′- and H-phase materials.

For other T′-MA_2N_4 systems, we find their HER performance will be improved by the strain engineering. Fig. 8(c) displays the variation of ΔG_H^* versus the tensile strain (ε) for T′-phase $MoSi_2N_4$, WSi_2N_4, and WGe_2N_4 nanosheets. It can be seen that ΔG_H^* of T′-WGe_2N_4 will drop to the zero point under a strain of ε=0.04. For the T′-$MoSi_2N_4$ and T′-WSi_2N_4 systems, their ΔG_H^* values can also be modulated, which are below 0.2 eV when ε is larger than 0.04 and 0.06 and reach the zero point under the stain of ε=0.06 and 0.08, respectively. Note that all the T′-MA_2N_4 nanosheets with good HER activity are metallic, which will be desirable for the HER applications. It would be mentioned that the reduction of ΔG_H^* in these strained T′-MA_2N_4 nanosheets can be explained by the up-shift of p-band centre of the surface N atoms (ϵ_{N-2p}). A linear relationship between the ΔG_H^* and ϵ_{N-2p} can be visualized in the inset of Fig. 8(c) and more detailed data are present in the Fig. S1 of supplementary material. Based on the calculated ΔG_H^* data, the exchange current density (i_0) is evaluated as $i_0 = -ek_0/(1 + e^{\frac{|\Delta G_H^*|}{k_B T}})$. Following the previous work [16,18], the rate constant k_0 is set to 1 and k_B is the Boltzmann constant. The corresponding volcano curve of $log(i_0)$ versus ΔG_H^* is depicted in Fig. 8(d). Clearly, the strain-free T′-$MoGe_2N_4$ and strained T′-MA_2N_4 nanosheets appear at the volcano peak, which demonstrates they possess the best HER activity. Therefore, these T′-MA_2N_4 nanosheets will be promising candidate catalysts for the HER, which have potential applications in the renewable and green energy fields.

H-to-T′ phase transition

Currently, for the MA_2N_4 systems, only the H-phase geometry has been experimentally fabricated [1,8]. Thus, we further explore the possible H-to-T′ phase transition in the MA_2N_4 (M=Mo/W, A=Si/Ge) nanosheets. According to the previous work of MoS_2 systems, the H-to-T′ phase transition will be triggered by the electron injection of about 0.6 e per formula unit (e/f.u.) [63,64]. To this end, we also calculate the energy difference between the T′- and H-MA_2N_4 systems ($E(T') - E(H)$) versus the amount of additional electrons (ΔQ). Here, a positive (negative) $E(T') - E(H)$ value means the H(T′)-phase is energetically favourable. It would be noticed for the T′-MA_2N_4 nanosheets, the structural distortions not only occur in the central MN_2 part but also appear in the surface AN layers. The Si/Ge atoms, which directly connect to the inner N atoms, are also buckled with a buckling height (Δh_A) of about 0.14~0.23 Å in Table 1. Thus, the energetic cost of H-to-T′ phase transition will be larger in the MA_2N_4 nanosheets than the MoS_2 one. Since the $E(T') - E(H)$ values are large at the neutral state as shown in Fig. 9(a), the required ΔQ for the H-to-T′ phase transition in the MA_2N_4 systems will be high. For the $MoGe_2N_4$ and WGe_2N_4 nanosheets, the critical ΔQ of $E(T') - E(H) = 0$ is as large as 1.25 and 1.45 e/f.u., which are about twice the value of MoS_2 system. For the $MoSi_2N_4$ and WSi_2N_4 nanosheets, the critical ΔQ value is even beyond 1.5 e/f.u. as indicated in Fig. 9(a). Such high electron injection concentrations will be hard to be achieved in the experiment. Thus, in the current experiments, the T′-MA_2N_4 nanosheets have not been observed yet.

It has been reported that in addition to the charge doping, the strain engineering also facilitates the synthesis of metastable T′-phase structures [65]. Here, the $MoGe_2N_4$ nanosheet, which has the smallest $E(T') - E(H)$ and best HER performance, is chosen as a representative to investigate the strain effect on the H-to-T′ phase transition. Fig. 9(b) displays the variation of $E(T') - E(H)$ as a function of lattice constants for the $MoGe_2N_4$ systems. It can be seen that the $E(T') - E(H)$ values are declined with the increase of lattice constants. The T′-phase structure will become energetically preferred to the H-phase one under sufficient long a or b lattice constants. It implies that the required electron amount for the H-to-T′ transition will be diminished in presence of tensile strain. Actually, when a 10% biaxial tensile strain is applied to the $MoGe_2N_4$ nanosheet, the critical ΔQ for the $E(T') - E(H) = 0$ is substantially lowered to 0.4 e/f.u. as shown in Fig. 9(a), which is only 1/3 of the strain-free value. Such required additional charges in the strained MA_2N_4 systems are comparable to the MoS_2 case. For the H-MA_2N_4 systems, previous theoretical works have suggested they will endure the large biaxial tensile strains up to 18 ~19.5% [66,67]. Thus, for the largely strained H-phase MA_2N_4 systems, a certain small amount of charge injection will bring the H-to-T′ phase transition. The

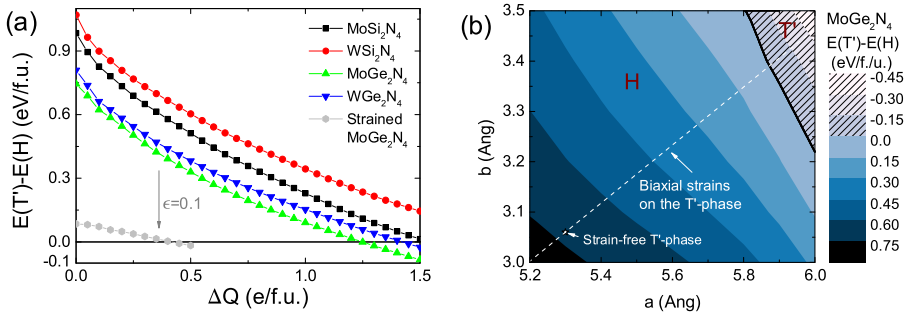

Fig. 9. (a) The variations of energy differences between the T′- and H-MA_2N_4 nanosheets versus the amount of electron injection. (b) The contour map of the energy differences between the T′- and H-$MoGe_2N_4$ nanosheets with different lattice constants.

T′-MA_2N_4 systems will be possibly fabricated via a combined effect of electron injection and tensile strain on the H-phase ones.

4. Conclusion

In summary, we have performed a comprehensive study on the structural, mechanical, electronic and catalytic properties of T′-phase MA_2N_4 (M=Mo/W, A=Si/Ge) nanosheets. We find that (1) owing to the constraint of the surface layers, the dimerization-induced structural distortion is weaker in the T′-MA_2N_4 nanosheets than in the common T′-phase TMDs. Sufficient stability is confirmed in these T′-MA_2N_4 nanosheets from the energetic, dynamical, thermal and mechanical points of view, which can maintain the free-standing form at room temperature. (2) Compared to the H-phase MA_2N_4 ones, these T′-MA_2N_4 nanosheets are slightly softer and have an anisotropic mechanical behaviour. Different from the semiconducting H-phase counterparts, the T′-MA_2N_4 nanosheets will exhibit a semimetallic or metallic behaviour depending on the lattice constants. (3) Excellent HER performance is revealed in these T′-phase systems. The Gibbs free energy ΔG_H^* is close to the ideal zero point in the strain-free T′-$MoGe_2N_4$ nanosheet, and for other T′-MA_2N_4 systems, the ΔG_H^* values can also be tuned to zero by the strain engineering. Moreover, all the surface N atoms of T′-MA_2N_4 nanosheets are active sites for the HER and the HER activity can be maintained over a wider range of H concentrations, which is superior to the MoS_2 system. (4) Possible H-to-T′ phase transition has been examined for the MA_2N_4 nanosheets. Unlike MoS_2, the phase transition will be hardly triggered by the electron injection alone, but the T′-phase will become energetically preferred to the H-phase via a combined effect of electron injection and tensile strain. Our study demonstrates that the T′-phase MA_2N_4 nanosheets exhibit peculiar electronic properties and excellent HER performance, which endows them promising applications in nanoelectronics, nano-devices, and renewable energy fields.

CRediT authorship contribution statement

Yi Ding: Conceptualization, Methodology, Writing – original draft. **Yanli Wang:** Software, Writing – review & editing.

Declaration of competing interest

The authors declare that they have no known competing financial interests or personal relationships that could have appeared to influence the work reported in this paper.

Data availability

Data will be made available on request.

Acknowledgements

The authors acknowledge the support from the National Natural Science Foundation of China (11774312) and the special support project for high-level talents in Hangzhou.

Appendix A. Supplementary data

Supplementary material related to this article can be found online at https://doi.org/10.1016/j.apsusc.2023.157256.

References

[1] Y.-L. Hong, Z. Liu, L. Wang, T. Zhou, W. Ma, C. Xu, S. Feng, L. Chen, M.-L. Chen, D.-M. Sun, X.-Q. Chen, H.-M. Cheng, W. Ren, Chemical vapor deposition of layered two-$MoSi_2N_4$ materials, Science 369 (6504) (2020) 670–674, http://dx.doi.org/10.1126/science.abb7023.

[2] K.S. Novoselov, Discovery of 2D van der Waals layered $MoSi_2N_4$ family, Natl. Sci. Rev. 7 (12) (2020) 1842–1844, http://dx.doi.org/10.1093/nsr/nwaa190.

[3] L. Wang, Y. Shi, M. Liu, A. Zhang, Y.-L. Hong, R. Li, Q. Gao, M. Chen, W. Ren, H.-M. Cheng, Y. Li, X.-Q. Chen, Intercalated architecture of MA_2Z_4 family layered van der Waals materials with emerging topological, magnetic and superconducting properties, Nature Commun. 12 (1) (2021) 2361, http://dx.doi.org/10.1038/s41467-021-22324-8.

[4] C. Lin, X. Feng, D. Legut, X. Liu, Z.W. Seh, R. Zhang, Q. Zhang, Discovery of efficient visible-light driven oxygen evolution photocatalysts: Automated high-throughput computational screening of MA_2Z_4, Adv. Funct. Mater. 32 (45) (2022) 2207415, http://dx.doi.org/10.1002/adfm.202207415.

[5] A. Yadav, J. Kangsabanik, N. Singh, A. Alam, Novel two-dimensional MA_2N_4 materials for photovoltaic and spintronic applications, J. Phys. Chem. Lett. 12 (41) (2021) 10120–10127, http://dx.doi.org/10.1021/acs.jpclett.1c02650.

[6] Y. Ding, Y. Wang, Computational exploration of stable 4d/5d transition-metal MSi_2N_4 (M=Y-Cd and Hf-Hg) nanosheets and their versatile electronic and magnetic properties, J. Phys. Chem. C 125 (2021) 19580–19591.

[7] Y.-T. Ren, L. Hu, Y.-T. Chen, Y.-J. Hu, J.-L. Wang, P.-L. Gong, H. Zhang, L. Huang, X.-Q. Shi, Two-dimensional MSi_2N_4 monolayers and van der Waals heterostructures: Promising spintronic properties and band alignments, Phys. Rev. Mater. 6 (6) (2022) 064006, http://dx.doi.org/10.1103/physrevmaterials.6.064006.

[8] D. Huang, F. Liang, R. Guo, D. Lu, J. Wang, H. Yu, H. Zhang, $MoSi_2N_4$: A 2D regime with strong exciton-phonon coupling, Adv. Opt. Mater. 10 (2022) 2102612, http://dx.doi.org/10.1002/adom.202102612.

[9] B. Mortazavi, B. Javvaji, F. Shojaei, T. Rabczuk, A.V. Shapeev, X. Zhuang, Exceptional piezoelectricity, high thermal conductivity and stiffness and promising photocatalysis in two-dimensional $MoSi_2N_4$ family confirmed by first-principles, Nano Energy 82 (2021) 105716, http://dx.doi.org/10.1016/j.nanoen.2020.105716.

[10] A. Priydarshi, Y.S. Chauhan, S. Bhowmick, A. Agarwal, Large and anisotropic carrier mobility in monolayers of the MA_2Z_4 series (M=Cr, Mo, W; A=Si, Ge; and Z=N, P), Nanoscale 14 (33) (2022) 11988–11997, http://dx.doi.org/10.1039/d2nr02382b.

[11] A. Bafekry, M. Faraji, D.M. Hoat, M. Shahrokhi, M.M. Fadlallah, F. Shojaei, S.A.H. Feghhi, M. Ghergherehchi, D. Gogova, $MoSi_2N_4$ single-layer: a novel two-dimensional material with outstanding mechanical, thermal, electronic and optical properties, J. Phys. D: Appl. Phys. 54 (15) (2021) 155303, http://dx.doi.org/10.1088/1361-6463/abdb6b.

[12] Y. Wu, Z. Tang, W. Xia, W. Gao, F. Jia, Y. Zhang, W. Zhu, W. Zhang, P. Zhang, Prediction of protected band edge states and dielectric tunable quasiparticle and excitonic properties of monolayer MoSi2N4, npj Comput. Mater. 8 (1) (2022) http://dx.doi.org/10.1038/s41524-022-00815-6.

[13] Q. Wang, L. Cao, S.-J. Liang, W. Wu, G. Wang, C.H. Lee, W.L. Ong, H.Y. Yang, L.K. Ang, S.A. Yang, Y.S. Ang, Efficient ohmic contacts and built-in atomic sublayer protection in $MoSi_2N_4$ and WSi_2N_4 monolayers, npj 2D Mater. Appl. 5 (1) (2021) 71, http://dx.doi.org/10.1038/s41699-021-00251-y.

[14] J. Huang, P. Li, X. Ren, Z.-X. Guo, Promising properties of a sub-5-nm monolayer $MoSi_2N_4$ transistor, Phys. Rev. Appl. 16 (4) (2021) 044022, http://dx.doi.org/10.1103/physrevapplied.16.044022.

[15] X. Sun, Z. Song, N. Huo, S. Liu, C. Yang, J. Yang, W. Wang, J. Lu, Performance limit of monolayer $MoSi_2N_4$ transistors, J. Mater. Chem. C 9 (41) (2021) 14683–14698, http://dx.doi.org/10.1039/d1tc02937a.

[16] Y. Zang, Q. Wu, W. Du, Y. Dai, B. Huang, Y. Ma, Activating electrocatalytic hydrogen evolution performance of two-dimensional MSi_2N_4(M=Mo, W) : A theoretical prediction, Phys. Rev. Mater. 5 (4) (2021) 045801, http://dx.doi.org/10.1103/physrevmaterials.5.045801.

[17] W. Qian, Z. Chen, J. Zhang, L. Yin, Monolayer MoSi2N4- as promising electrocatalyst for hydrogen evolution reaction: A DFT prediction, J. Mater. Sci. Technol. 99 (2022) 215–222, http://dx.doi.org/10.1016/j.jmst.2021.06.004.

[18] C. Xiao, R. Sa, Z. Cui, S. Gao, W. Du, X. Sun, X. Zhang, Q. Li, Z. Ma, Enhancing the hydrogen evolution reaction by non-precious transition metal (non-metal) atom doping in defective $MoSi_2N_4$ monolayer, Appl. Surf. Sci. 563 (2021) 150388, http://dx.doi.org/10.1016/j.apsusc.2021.150388.

[19] W. Shi, G. Yin, S. Yu, T. Hu, X. Wang, Z. Wang, Atomic precision tailoring of two-dimensional MoSi2N4 as electrocatalyst for hydrogen evolution reaction, J. Mater. Sci. 57 (39) (2022) 18535–18548, http://dx.doi.org/10.1007/s10853-022-07755-y.

[20] S. Lu, Y. Zhang, F. Lou, K. Guo, Z. Yu, Non-precious metal activated MoSi2N4 monolayers for high-performance OER and ORR electrocatalysts: A first-principles study, Appl. Surf. Sci. 579 (2022) 152234, http://dx.doi.org/10.1016/j.apsusc.2021.152234.

[21] T. Tong, Y. Linghu, G. Wu, C. Wang, C. Wu, Nitric oxide electrochemical reduction reaction on transition metal-doped $MoSi_2N_4$ monolayers, Phys. Chem. Chem. Phys. 24 (31) (2022) 18943–18951, http://dx.doi.org/10.1039/d2cp01500e.

[22] X. Sun, J. Zheng, Z. Yao, S. Deng, Z. Pan, S. Wang, J. Wang, DFT investigation of single metal atom-doped 2D MA_2Z_4 materials for NO electrocatalytic reduction to NH_3, J. Phys. Chem. C 126 (41) (2022) 17598–17607, http://dx.doi.org/10.1021/acs.jpcc.2c05780.

[23] H. Guo, P. Yuan, J. Zhao, J. Zhao, Q. Peng, R. Song, First-principles studies of monolayers MoSi2N4 decorated with transition metal single-atom for visible light-driven high-efficient CO2 reduction by strain and electronic engineering, Chem. Eng. J. 450 (2022) 138198, http://dx.doi.org/10.1016/j.cej.2022.138198.

[24] Q. Dang, Y. Zhang, X. Wang, T. Liu, M. Zhang, X. Li, W. Guo, S. Tang, J. Jiang, Synergistic effect of a diatomic boron-doped layered two-dimensional MSi_2N_4 monolayer for an efficient electrochemical nitrogen reduction, J. Mater. Chem. A 10 (28) (2022) 14820–14827, http://dx.doi.org/10.1039/d2ta03667c.

[25] J. Chen, Q. Tang, The versatile electronic, magnetic and photo-electro catalytic activity of a new 2D MA_2Z_4 family, Chem. Eur. J. 27 (2021) 9925–9933., http://dx.doi.org/10.1002/chem.202100851.

[26] J. Zheng, X. Sun, J. Hu, S. Wang, Z. Yao, S. Deng, X. Pan, Z. Pan, J. Wang, Symbolic transformer accelerating machine learning screening of hydrogen and deuterium evolution reaction catalysts in MA_2Z_4 materials, ACS Appl. Mater. Interfaces 13 (43) (2021) 50878–50891, http://dx.doi.org/10.1021/acsami.1c13236.

[27] Y. Liu, Y. Ji, Y. Li, Multilevel theoretical screening of novel two-dimensional MA_2Z_4 family for hydrogen evolution, J. Phys. Chem. Lett. 12 (37) (2021) 9149–9154, http://dx.doi.org/10.1021/acs.jpclett.1c02487.

[28] W. Zhao, J. Pan, Y. Fang, X. Che, D. Wang, K. Bu, F. Huang, Metastable MoS_2: Crystal structure, electronic band structure, synthetic approach and intriguing physical properties, Chem. Eur. J. 24 (60) (2018) 15942–15954, http://dx.doi.org/10.1002/chem.201801018.

[29] Y.C. Liu, V. Wang, M.G. Xia, S.L. Zhang, First-principles study on structural, thermal, mechanical and dynamic stability of T'-MoS_2, J. Phys.: Condens. Matter 29 (9) (2017) 095702, http://dx.doi.org/10.1088/1361-648x/aa5213.

[30] F. Mehmood, R. Pachter, T.C. Back, J.J. Boeckl, R.T. Busch, P.R. Stevenson, Two-dimensional MoS_2 2H, 1T, and 1T′ crystalline phases with incorporated adatoms: theoretical investigation of electronic and optical properties, Appl. Opt. 60 (25) (2021) G232, http://dx.doi.org/10.1364/ao.433239.

[31] Z. Lai, Q. He, T.H. Tran, D.V.M. Repaka, D.-D. Zhou, Y. Sun, S. Xi, Y. Li, A. Chaturvedi, C. Tan, B. Chen, G.-H. Nam, B. Li, C. Ling, W. Zhai, Z. Shi, D. Hu, V. Sharma, Z. Hu, Y. Chen, Z. Zhang, Y. Yu, X.R. Wang, R.V. Ramanujan, Y. Ma, K. Hippalgaonkar, H. Zhang, Metastable 1T′-phase group VIB transition metal dichalcogenide crystals, Nature Mater. 20 (8) (2021) 1113–1120, http://dx.doi.org/10.1038/s41563-021-00971-y.

[32] X. Qian, J. Liu, L. Fu, J. Li, Quantum spin Hall effect in two-dimensional transition metal dichalcogenides, Science 346 (6215) (2014) 1344–1347, http://dx.doi.org/10.1126/science.1256815.

[33] L. Lei, D. Huang, G. Zeng, M. Cheng, D. Jiang, C. Zhou, S. Chen, W. Wang, A fantastic two-dimensional MoS_2 material based on the inert basal planes activation: Electronic structure, synthesis strategies, catalytic active sites, catalytic and electronics properties, Coord. Chem. Rev. 399 (2019) 213020, http://dx.doi.org/10.1016/j.ccr.2019.213020.

[34] X. Zhang, S. Hua, L. Lai, Z. Wang, T. Liao, L. He, H. Tang, X. Wan, Strategies to improve electrocatalytic performance of MoS_2-based catalysts for hydrogen evolution reactions, RSC Adv. 12 (28) (2022) 17959–17983, http://dx.doi.org/10.1039/d2ra03066g.

[35] J. Chen, F. Li, Y. Tang, Q. Tang, Tuning the phase stability and surface HER activity of 1T′-MoS_2 by covalent chemical functionalization, J. Mater. Chem. C 8 (44) (2020) 15852–15859, http://dx.doi.org/10.1039/d0tc03943h.

[36] J. Ekspong, E. Gracia-Espino, Theoretical analysis of surface active sites in defective 2H and 1T′ MoS_2 polymorphs for hydrogen evolution reaction: Quantifying the total activity of point defects, Adv. Theory Simul. 3 (3) (2020) 1900213, http://dx.doi.org/10.1002/adts.201900213.

[37] Y. Yu, G.-H. Nam, Q. He, X.-J. Wu, K. Zhang, Z. Yang, J. Chen, Q. Ma, M. Zhao, Z. Liu, F.-R. Ran, X. Wang, H. Li, X. Huang, B. Li, Q. Xiong, Q. Zhang, Z. Liu, L. Gu, Y. Du, W. Huang, H. Zhang, High phase-purity 1T′-MoS_2- and 1T′-$MoSe_2$-layered crystals, Nature Chem. 10 (6) (2018) 638–643, http://dx.doi.org/10.1038/s41557-018-0035-6.

[38] Y. Cao, Roadmap and direction toward high-performance MoS_2 hydrogen evolution catalysts, ACS Nano 15 (7) (2021) 11014–11039, http://dx.doi.org/10.1021/acsnano.1c01879.

[39] G. Kresse, J. Furthmüller, Efficient iterative schemes for ab initio total-energy calculations using a plane-wave basis set, Phys. Rev. B 54 (1996) 11169–11186, http://dx.doi.org/10.1103/PhysRevB.54.11169, URL https://link.aps.org/doi/10.1103/PhysRevB.54.11169.

[40] G. Kresse, J. Furthmüller, Efficiency of ab-initio total energy calculations for metals and semiconductors using a plane-wave basis set, Comput. Mater. Sci. 6 (1) (1996) 15–50, http://dx.doi.org/10.1016/0927-0256(96)00008-0.

[41] P. Wisesa, K.A. McGill, T. Mueller, Efficient generation of generalized Monkhorst–Pack grids through the use of informatics, Phys. Rev. B 93 (2016) 155109, http://dx.doi.org/10.1103/PhysRevB.93.155109, URL https://link.aps.org/doi/10.1103/PhysRevB.93.155109.

[42] V. Wang, N. Xu, J.-C. Liu, G. Tang, W.-T. Geng, VASPKIT: A user-friendly interface facilitating high-throughput computing and analysis using VASP code, Comput. Phys. Comm. 267 (2021) 108033, http://dx.doi.org/10.1016/j.cpc.2021.108033.

[43] G. Pizzi, V. Vitale, R. Arita, S. Blgel, F. Freimuth, G. Géranton, M. Gibertini, D. Gresch, C. Johnson, T. Koretsune, J. Ibañez-Azpiroz, H. Lee, J.-M. Lihm, D. Marchand, A. Marrazzo, Y. Mokrousov, J.I. Mustafa, Y. Nohara, Y. Nomura, L. Paulatto, S. Poncé, T. Ponweiser, J. Qiao, F. Thle, S.S. Tsirkin, M. Wierzbowska, N. Marzari, D. Vanderbilt, I. Souza, A.A. Mostofi, J.R. Yates, Wannier90 as a community code: new features and applications, J. Phys.: Condens. Matter 32 (16) (2020) 165902, http://dx.doi.org/10.1088/1361-648x/ab51ff.

[44] Q. Wu, S. Zhang, H.-F. Song, M. Troyer, A.A. Soluyanov, WannierTools : An open-source software package for novel topological materials, Comput. Phys. Comm. 224 (2018) 405–416, http://dx.doi.org/10.1016/j.cpc.2017.09.033, URL http://www.sciencedirect.com/science/article/pii/S0010465517303442.

[45] J. Rossmeisl, Z.-W. Qu, H. Zhu, G.-J. Kroes, J. Nørskov, Electrolysis of water on oxide surfaces, J. Electroanal. Chem. 607 (1–2) (2007) 83–89, http://dx.doi.org/10.1016/j.jelechem.2006.11.008.

[46] E. Caldeweyher, J.-M. Mewes, S. Ehlert, S. Grimme, Extension and evaluation of the D4 London-dispersion model for periodic systems, Phys. Chem. Chem. Phys. 22 (16) (2020) 8499–8512, http://dx.doi.org/10.1039/d0cp00502a.

[47] J. Rumble, CRC Handbook of Chemistry and Physics, hundred and third ed., CRC Press, 2022.

[48] K. Chen, J. Deng, D. Kan, Y. Yan, Q. Shi, W. Huo, M. Song, S. Yang, J.Z. Liu, Ferromagnetic and nonmagnetic 1T' charge density wave states in transition metal dichalcogenides: Physical mechanisms and charge doping induced reversible transition, Phys. Rev. B 105 (2022) 024414, http://dx.doi.org/10.1103/PhysRevB.105.024414, URL https://link.aps.org/doi/10.1103/PhysRevB.105.024414.

[49] A. Togo, I. Tanaka, First principles phonon calculations in materials science, Scr. Mater. 108 (2015) 1–5.

[50] B. Özdamar, G. Özbal, M.N. Çınar, K. Sevim, G. Kurt, B. Kaya, H. Sevinçli, Structural, vibrational, and electronic properties of single-layer hexagonal crystals of group IV and V elements, Phys. Rev. B 98 (4) (2018) http://dx.doi.org/10.1103/physrevb.98.045431.

[51] T. Cao, Z. Li, S.G. Louie, Tunable magnetism and half-metallicity in hole-doped monolayer GaSe, Phys. Rev. Lett. 114 (23) (2015) 236602, http://dx.doi.org/10.1103/physrevlett.114.236602.

[52] E. Cadelano, P.L. Palla, S. Giordano, L. Colombo, Elastic properties of hydrogenated graphene, Phys. Rev. B 82 (2010) 235414, http://dx.doi.org/10.1103/PhysRevB.82.235414, URL https://link.aps.org/doi/10.1103/PhysRevB.82.235414.

[53] S. Imani Yengejeh, W. Wen, Y. Wang, Mechanical properties of lateral transition metal dichalcogenide heterostructures, Front. Phys. 16 (1) (2021) 13502.

[54] X. Li, X. Wu, J. Yang, Half-metallicity in $MnPSe_3$ exfoliated nanosheet with carrier doping, J. Am. Chem. Soc. 136 (31) (2014) 11065–11069, http://dx.doi.org/10.1021/ja505097m.

[55] Y. Wang, Y. Ding, A first-principles study of a real energetically stable MoN_2 nanosheet and its tunable electronic structure, J. Mater. Chem. C 6 (9) (2018) 2245–2251, http://dx.doi.org/10.1039/c7tc05717b.

[56] F. Mouhat, F.-X. Coudert, Necessary and sufficient elastic stability conditions in various crystal systems, Phys. Rev. B 90 (2014) 224104, http://dx.doi.org/10.1103/PhysRevB.90.224104, URL https://link.aps.org/doi/10.1103/PhysRevB.90.224104.

[57] Y. Wang, Y. Ding, Stable puckered C_2N_2 nanosheet with giant anisotropic hole carrier mobility: insights from first-principles, J. Mater. Chem. C 8 (44) (2020) 15655–15663, http://dx.doi.org/10.1039/d0tc03814h.

[58] D.K. Pham, Electronic properties of a two-dimensional van der Waals MoGe_2N_4/MoSi_2N_4 heterobilayer: effect of the insertion of a graphene layer and interlayer coupling, RSC Adv. 11 (46) (2021) 28659–28666, http://dx.doi.org/10.1039/d1ra04531h.

[59] Y. Ding, Y. Wang, First-principles study of two-dimensional $MoN_2X_2Y_2$ (X=B-In, Y=N-Te) nanosheets: The III–VI analogues of $MoSi_2N_4$ with peculiar electronic and magnetic properties, Appl. Surf. Sci. 593 (2022) 153317, http://dx.doi.org/10.1016/j.apsusc.2022.153317, URL https://www.sciencedirect.com/science/article/pii/S0169433222008728.

[60] R. Islam, R. Verma, B. Ghosh, Z. Muhammad, A. Bansil, C. Autieri, B. Singh, Switchable large-gap quantum spin Hall state in the two-dimensional MSi_2Z_4 class of materials, Phys. Rev. B 106 (24) (2022) 245149, http://dx.doi.org/10.1103/physrevb.106.245149.

[61] Y. Wang, Y. Ding, The hydrogen-induced structural stability and promising electronic properties of molybdenum and tungsten dinitride nanosheets: a first-principles study, J. Mater. Chem. C 4 (31) (2016) 7485–7493, http://dx.doi.org/10.1039/c6tc02161a.

[62] M. Yu, D.R. Trinkle, Accurate and efficient algorithm for Bader charge integration, J. Chem. Phys. 134 (6) (2011) 064111, http://dx.doi.org/10.1063/1.3553716.

[63] X.-H. Lv, M.-Q. Wu, Y.-T. Ren, R.-N. Wang, H. Zhang, C.-D. Jin, R.-Q. Lian, P.-L. Gong, X.-Q. Shi, J.-L. Wang, Hole- and electron-injection driven phase transitions in transition metal dichalcogenides and beyond: A unified understanding, Phys. Rev. B 105 (2022) 024108, http://dx.doi.org/10.1103/PhysRevB.105.024108, URL https://link.aps.org/doi/10.1103/PhysRevB.105.024108.

[64] X. Ji, C. Wu, J. Deng, J. Li, C. Jin, Reversible H-T′ phase transition in monolayer molybdenum disulfide via electron beam assisted solid state lithiation/delithiation, Appl. Phys. Lett. 116 (3) (2020) 033103, http://dx.doi.org/10.1063/1.5125312.

[65] M.S. Sokolikova, C. Mattevi, Direct synthesis of metastable phases of 2D transition metal dichalcogenides, Chem. Soc. Rev. 49 (2020) 3952–3980, http://dx.doi.org/10.1039/D0CS00143K.

[66] Q. Li, W. Zhou, X. Wan, J. Zhou, Strain effects on monolayer $MoSi_2N_4$: Ideal strength and failure mechanism, Physica E 131 (2021) 114753, http://dx.doi.org/10.1016/j.physe.2021.114753.

[67] H. Alavi-Rad, Strain engineering in optoelectronic properties of $MoSi_2N_4$ monolayer: ultrahigh tunability, Semicond. Sci. Technol. 37 (6) (2022) 065018, http://dx.doi.org/10.1088/1361-6641/ac6769.